Burst pressure prediction of cord-rubber composite structures using global–local nonlinear finite element analysis

Bhosale, Ahaan; Barendse, Rob; Chen, Boyang; van Campen, J. M.J.F.

DOI
10.1016/j.compositesa.2024.108361

Publication date
2024

Document Version
Final published version

Published in
Composites Part A: Applied Science and Manufacturing

Composites: Part A 185 (2024) 108361

Contents lists available at ScienceDirect

Composites Part A

journal homepage: www.elsevier.com/locate/compositesa

Burst pressure prediction of cord-rubber composite structures using global–local nonlinear finite element analysis

Ahaan Bhosale [a,b], Rob Barendse [b], Boyang Chen [a,*], J.M.J.F. van Campen [a]

[a] Department of Aerospace Structures & Materials, Faculty of Aerospace Engineering, Delft University of Technology, Kluyverweg 1, Delft, 2629 HS, The Netherlands

[b] TANIQ BV., Sydneystraat 112, Rotterdam, 3047 BP, The Netherlands

ARTICLE INFO

Keywords:
Rubber composite
Filament winding
Multiscale modeling
Burst pressure

ABSTRACT

This study aims to develop a model to predict the burst pressure of a dry filament wound cord-rubber composite pressure vessel under hydrostatic internal pressurization using a submodelling based global–local FEA model. The model links the global displacements of a rebar-based model to obtain the local deformation state in a single rhomboidal representative volume. Emphasis is placed on capturing the local stress concentrations in the fibers due to the unique filament winding mosaic pattern. Fiber damage is included in the local model using a maximum principle strain criteria. Verification of the created model is done experimentally on industrially manufactured burst-test specimens. Measurements for displacement during the experiments are taken photographically, while the burst pressure is captured using a pressure transducer. The final error between the burst pressure of the samples and the experimental demonstrators is approximately 6.5%, a marked improvement over conventional models with truss and rebar elements as fibers.

1. Introduction

Cord-rubber composites (CRCs) are an interesting branch of composites that use highly tough and flexible rubber elastomers as the matrix material while using stiff twisted cord constructions as main load-bearing members. Usually, these structures are used under internal pressurization such that the rubber with its low elastic modulus and high failure strain provides flexibility and acts as a leak-proof barrier, while the high-modulus reinforcing cords provide the needed load-carrying capacity. These properties allow these composites to be used in some of the most demanding applications, where large deformations should be sustained without product failure.

For cord rubber composites, homogenization-based approaches have commonly been used to obtain the continuum behavior of the structure. Linear-elastic homogenization methods such as those presented by Akasaka and Hirano [1], Clark [2] and Ford [3] suffer from the obvious drawback of not being able to accurately model elastomeric structures under large deformations due to the hyperelastic nature of the rubber and some twisted cords. Several hyperelastic continuum models developed specifically to describe highly nonlinear reinforced composites solve this problem by employing Spencer's constitutive theory [4] for anisotropic solid continua. These include models developed for biological tissues [5–9], for woven fabric–rubber composites [10], and for fabric–rubber composites [11,12]. These models reasonably represent the continuum behavioral characteristics of the composite, but due to their phenomenological nature, need experimental campaigns to calibrate the response new fiber/matrix combinations, along with modeling their damage. They are also unable to capture highly local phenomena relevant to damage due to their homogenized nature.

The local effects due to the fiber overlaps can be included if the fiber overlap pattern itself is modeled. For cylindrical structures, it was demonstrated that modeling the mosaic pattern is critical to capture the stress state in a filament wound laminate [13]. This was further demonstrated experimentally by showcasing that the undulating area within a laminate can greatly lower its burst pressure [14]. Such overlap patterns, especially if modeled over the entire domain, can quickly get difficult to compute and expensive to simulate. Modeling such domains as unit cells or representative volume elements (RVEs) is a common strategy taken for tape-wound structures [15–17]. These studies often model the fiber overlap using empirical mathematical functions instead of modeling the geometry exactly. While an elegant solution for reducing computational cost, it must be understood that these approximations are more difficult to make for dry wound fiber bundles. Wet winding usually includes dipping the fibers in a resin bath which aids inter-fiber adhesion. As this is not the case in dry-wound fiber bundles, they are not able to adhere to previously laid down fiber

* Corresponding author.
E-mail address: B.Chen-2@tudelft.nl (B. Chen).

https://doi.org/10.1016/j.compositesa.2024.108361
Received 4 May 2024; Received in revised form 1 July 2024; Accepted 9 July 2024
Available online 19 July 2024

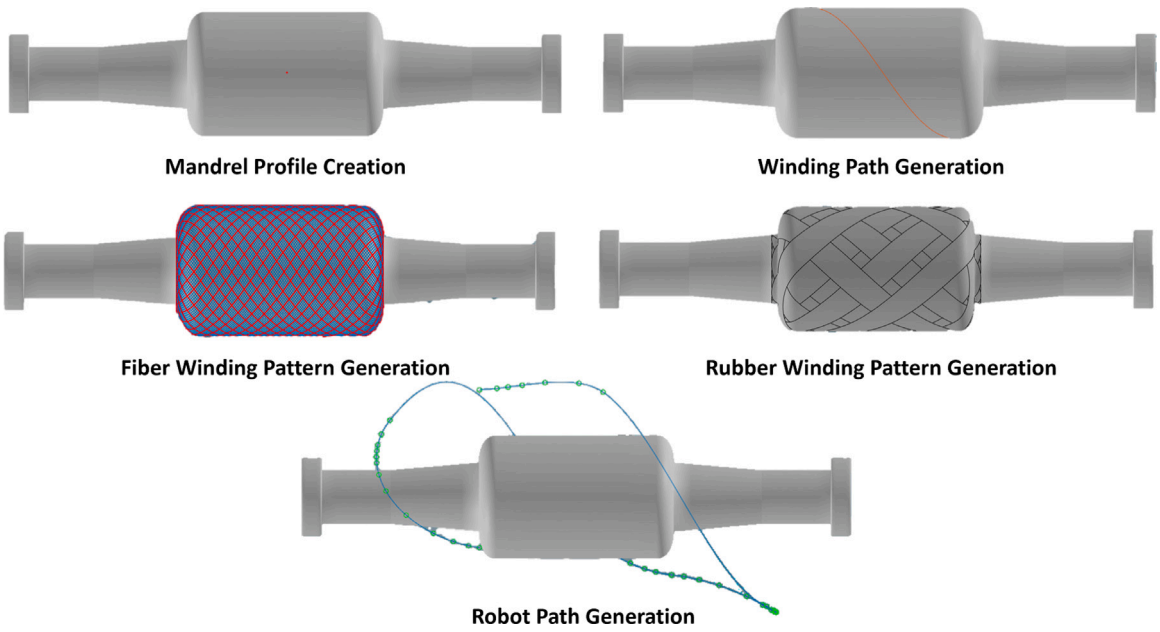

Fig. 1. Manufacturing steps using TaniqWind.

bundles and hence tend to 'bridge' under tension leading to a lack of compaction. Additionally, depending on the winding pattern chosen, filament wound structures may have fairly large unit cells. These unit cells cannot be approximated as flat structures, and the inclusion of mandrel curvature is necessary.

To model damage in rubber composites, extensive research attention has focused on fatigue modeling to capture phenomena such as fatigue, hysteresis, and the viscoelastic nature of rubber [18–22]. The modeling of single-cycle burst however is usually more dependent on the properties of the cord rather than that of the rubber, with factors such as fiber placement and fiber stiffness influencing the behavior of the composite [23]. Thus, there is a need to model the cord pattern in the CRC structure precisely to predict the burst pressure accurately.

In this study, a geometrical model is developed for the creation of the fiber-overlap pattern. The failure behavior of the cord-rubber composite structure is then studied using FEA via a global–local sub-modelling approach. Here, the local model is an RVE with the developed fiber overlap structure, while the full field global model has the fibers modeled using continuum rebar elements. Fiber failure is included as a damage mode in the local model, which is then validated via experimental burst tests on filament wound rubber composite structures.

2. Problem description

2.1. Rubber composite specimen

A cylindrical tank was chosen for this study due to its simplicity and widespread use in the rubber-composite industry. Design and manufacturing of the rubber and fiber winding were achieved using TANIQ BV's TaniqWind software, along with the bundled 6-axis ABB robotic system. The steps for the production of the specimens can be seen in Fig. 1.

The winding design consists of an inner and outer rubber layer, between which a fiber layer is wound. For each layer, a helical winding path is first generated based on the required winding angle and turn-around zones. The path is then repeated multiple times to form a winding pattern. Finally, the software outputs the machine paths, which can be exported to the robot for production. Post winding, a highly-tensioned nylon tape is wound around the mandrel to compact the laminate, after which it is placed in an oven for vulcanization.

For the current study, a single fiber layer was used sandwiched between two rubber layers. This marks the simplest possible configuration for a CRC filament wound tank. A neutral helical winding angle of $\pm 54.74°$ [24] was chosen for the fibers. This ensures that the cylindrical region undergoes minimal fiber rotation on loading and allows the cylindrical portion of the mandrel to be considered uniformly loaded. This is essential for the representative volume approach that this study will follow. A winding path with this angle allows for fibers to experience only axial stresses, thus negating the need for re-orientation. Winding was also done using a geodesic path, which is the shortest path between two points on the mandrel surface. This characteristic also means that the path is stable without the need for winding friction, and is hence non-slip [25].

The used fiber winding pattern is shown in Fig. 3(b). The fiber coverage for the design is 50.39%.

2.2. Materials and test data

The composite structure used consisted of a natural rubber matrix (NR60 compound, QEW Rubber Engineered Rubber, Netherlands) and an RFL-dipped polyamide 66 cord construction (1880 dtex/2 110Z).

The rubber compound was tested in uniaxial tension, planar tension, and biaxial tension at Axel Products, Inc, USA. For each testing mode, 3 specimens were used, and were loaded at a strain rate of 0.01 to mimic quasi-static conditions. Specimens in uniaxial tension were tested up to 250% strain, while biaxial and planar tension specimens were tested up to 100% and 60% strain respectively. The required specimens for each test were die-cut from a 150 mm X 150 mm sheet of the vulcanized rubber compound. Uniaxial tensile tests to failure were conducted on the cord constructions following ASTM-D885 [26] at the faculty of aerospace engineering, TU Delft, Netherlands.

The tensile fiber tests were performed on the 250 kN Zwick Roell test bench with a contact extensometer at the faculty of Aerospace Engineering, TU Delft. ASTM-D885/D885M [26], a standard specific to the tensile characterization of coated cords for placement in rubber, was used to define the parameters for the tests. Standard spiral grips were used to avoid concentrating load near the clamped ends. The test data is shown in Fig. 2(b).

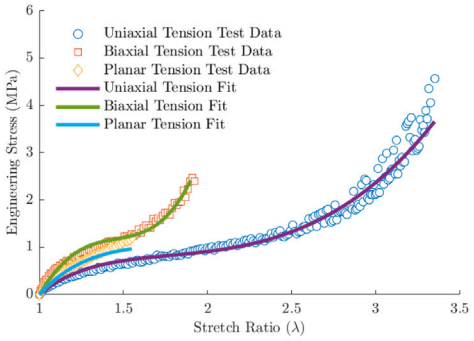

(a) Ogden hyperelastic model fit for rubber test data

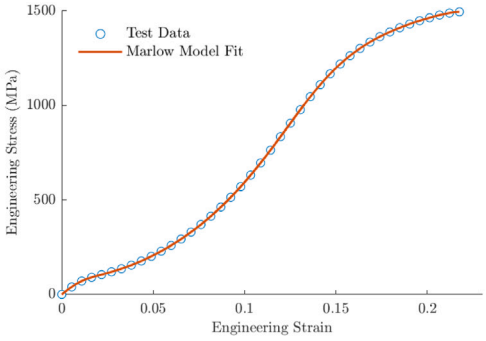

(b) Marlow hyperelastic model fit for cord test data

Fig. 2. Calibration of hyperelastic models to rubber and fiber test data.

Table 1
Calibrated constants for the 6th order Ogden model as shown in Eq. (1).

α_1	α_2	α_3	α_4	α_5	α_6
−0.131	0.503	4.828	−0.412	−1.471	−2.129
μ_1	μ_2	μ_3	μ_4	μ_5	μ_6
1.284	−7.760	0.103	16.172	−13.448	4.631

2.3. Material models

The 6-term Ogden hyperelastic model, as seen in Eq. (1) was used to calibrate the test data from all 3 test modes of the rubber into a single material model.

$$\Psi = \sum_{p=1}^{N} \frac{2\mu_p}{\alpha_p^2}\left(\lambda_1^{\alpha_p} + \lambda_2^{\alpha_p} + \lambda_3^{\alpha_p} - 3\right) \tag{1}$$

This model type was chosen as it has a proven track record for modeling rubbers accurately [5,27], benefits from data from multiple loading modes, and can capture all the non-linearities in the rubber response, including the 'upturn' in the stress–strain behavior. The calibrated data can be seen in Fig. 2(a) where the nominal stress is plotted against the stretch ratio ($\lambda = 1 + \epsilon_{nom}$). Excellent correlation is seen for uniaxial and biaxial tension (see Table 1 for the calibrated constants). For planar tension, a good correlation is seen for low stretch ratios. At higher ratios, the test no longer simulates a homogeneous strain state [27], and hence the fit is not relevant.

As seen in Fig. 2(b), the cords show a typical hyperelastic-like tensile response. It was theorized that the twisted structure itself, and the resulting interactions between filaments in the bundles were responsible for the unique non-linear response. The initial region shows an initially high but rapidly deteriorating stiffness due to the breakdown of the polymer coating on the twisted cords. This binder coating helps to transmit load and is a vital component in preventing the twisted cord from opening up under low loads. However, as tensile loads build up, the cord twist tightens up, and the twisted structure can transmit loads via inter-bundle friction. This is characterized by a rapid increase in stiffness. Finally, as the filaments approach their yield strength, another region of softening is observed in the response [28].

The Marlow material model [29] was used to calibrate the test data from the cords. The Marlow model is well suited to calibrate a hyperelastic model based on just uniaxial tensile test data as it is based solely on the first invariant (I_1) of the stretch tensor and hence is independent of a functional description of the strain energy density. This is shown in Eq. (2). A bonus of this calibration is that the exact stress–strain response is captured without needing additional curve fitting procedures.

$$\Psi = \Psi_{dev}\left(I_1\right) \tag{2}$$

2.4. Loads and boundary conditions

Fig. 10 shows the construction of the burst test rig. The specimen is internally pressurized by water up to failure. Water-tightness is ensured using a pair of metallic flanges on either end. On each flange pair, the upper and lower metallic flanges are bolted tightly together, thus sealing the polar opening of the specimen and forming a leak-proof connection. The sealing of the flanges is an important step in ensuring the water pressure is contained by the prototype on internal pressurization, and thus the bolts must be torqued adequately. During the test, the specimen is bolted securely to a test rig on one end, while being allowed to expand freely radially and axially at all other points.

3. Overlap pattern

3.1. Understanding the overlap pattern

A preliminary examination of the filament winding process helps to understand the generated overlap pattern. At its core, the fiber pattern is constructed using a continuous fiber yarn wrapped along an axisymmetric mandrel in a to-and-fro motion along the axis. The mandrel rotates about its independent axis. The relative difference in rotational and linear velocity of the mandrel and the robot head respectively allows for a precise definition of the path winding angle (α), which is defined as the angle the fiber makes with the meridian of the mandrel profile at each axial location — see Fig. 3(a).

Once a fiber path is generated, it is repeated along the mandrel's equatorial circumference to form a winding pattern that covers the mandrel surface by a predetermined coverage. Creating a pattern is essentially a play of finding an integer number of path repetitions that can result in the required fiber coverage [24].

On the cylindrical surface of the mandrel, the formed pattern consists of a repeating set of rhombi of varying sizes as seen in Fig. 3(b).

3.2. Overlap domain

For the context of this research, a distinction should be made between a repeating unit cell (RUC) and a representative volume element (RVE). A repeating unit cell is defined as the smallest structural unit that can be repeated along all axes to form the complete geometry. Analysis of RUCs is usually done with the help of periodic boundary conditions, which stipulate that corresponding nodes on opposite faces of an element should deform identically under an applied load [30]. These allow repeating unit cells (RUCs) to be studied independently while allowing the constraint of material continuity to be applied via relevant displacement boundary conditions. On the other hand, a representative volume element is the smallest volume in a structure with several constituent materials that can be considered to be statistically homogeneous such that the RVE response is characterized by

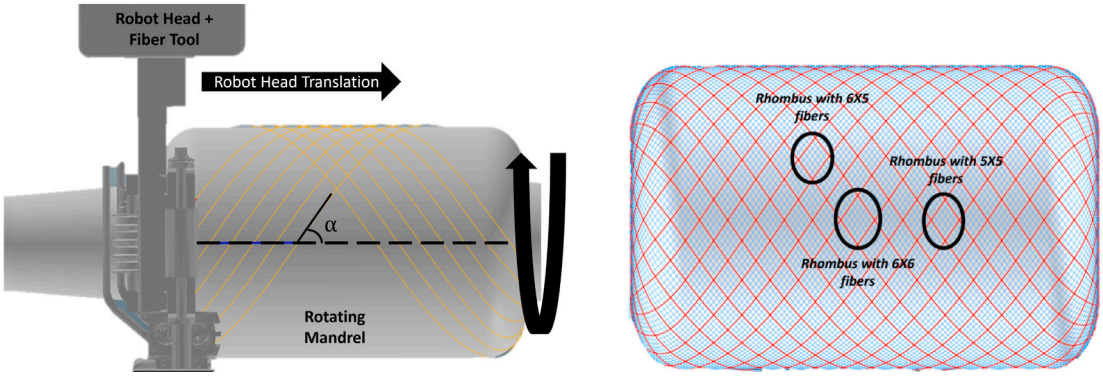

(a) Robotic winding process for path with winding angle α

(b) Three distinct rhombi developed during fiber winding

Fig. 3. The filament winding results in a repeating rhomboidal pattern to form with 3 distinct sizes.

the average response of all the constituents. In this manner, the RVE is considered representative of the entire structure. To be representative, it should be small enough such that the variation of the macroscopic fields it represents are sufficiently small, but yet should be large enough to be considered statistically homogeneous [31].

A rhomboidal unit cell as a result of the filament winding process can never be considered a pure RUC for the following reasons:

- Any filament winding pattern produced by TANIQ's winding platform will always have three distinct rhombus shapes. This leads to the variation in rhombi sizes as is seen in Fig. 3(b). Any attempt to find a truly repeating unit by combining several rhombi would either not be possible, or would lead to an RUC that is too big to benefit from the efficiency gains of the global–local approach.
- The overlap pattern itself does not follow a periodic pattern as neighboring rhombi can have completely different overlap patterns to a given rhombus. This means that no single 3D rhombus can be repeated along the axes to tile the mandrel surface while maintaining fiber continuity.

Instead, each rhombus can be considered as an RVE — with the assumption that each RVE contains features that represent the heterogeneity in the entire product domain. Following this line of thought, the logical pick amongst the three available rhombi to model as the RVE would be the one that is present most frequently in the pattern. Finding out the most common rhombus can be achieved via a simple arithmetic procedure:

- In filament winding, p describes the number of angular partitions in which the equator of the mandrel is divided. Divide the number of fiber loops n by the p number. The value m then represents the average number of fibers along one side of the rhombus.
- The remainder can be used as an indicator of the distribution of the 3 rhombi. The closer the remainder is to 1, the larger the number of $(m+1)\times(m+1)$ rhombi there will be. Similarly, the closer the remainder is to 0, the larger the number of $(m)\times(m)$ rhombi there will be.

For the chosen geometry, $p = 23$ and $n = 116$. It must be noted that only half of each boundary fiber (red fibers in Fig. 3(b)) contributes to the fiber count in a given rhombus as the other half is considered a part of the neighboring rhombus. Then, $m = 5\frac{1}{23}$. Thus, this shows that a very small portion of the rhombi will be larger than 5×5, and hence the 5×5 rhombus would be a reasonable choice for the RVE.

Based on the winding algorithm chosen, there can be 3 distinct rhombi that are formed in the fiber winding pattern — see Fig. 3(b). Based on the RVE approach, a submodel must be chosen that is most representative of the true volume. Thus, picking the most frequent rhombus in the pattern is a logical choice.

3.3. Overlap pattern generation

Reconstructing the overlap geometry with high precision is a complex engineering task. As seen in Fig. 4, overlapping fibers undergo bending, cross-sectional deformation, and also deviation from the intended helical path. Predicting this geometry requires detailed knowledge about the transverse material stiffness, the friction conditions at each overlap, and the cumulative deviation from the fiber path. To avoid this challenge, a simpler geometrical solution was employed, based on the observation that a cord under pure tension will travel the shortest path between any two points on which its ends lie.

For the overlap pattern, this means that when a fiber is laid on top of pre-existing fibers, the newly laid fiber will follow the shortest helical path around the fibers that are already laid such that it does not intersect any pre-existing geometry.

An elegant approach to automate the generation of crossover paths is the use of the convex hull algorithm. The convex hull $CH(Q)$ of a set of 2D planar points Q is defined as the convex polygon of the shortest perimeter which either contains or encloses all the points in Q [32]. Then, the set Q can be defined such that it contains a discretized set of all possible points the fiber can take. This includes circumferential points on both the mandrel and any other fibers previously laid down. $CH(Q)$ thus represents the shortest perimeter path the overlapping fiber takes over the mandrel and all previously laid fibers. All the points in $CH(Q)$ are then connected via straight lines to form the overlapping fiber paths.

This implementation can be seen in 2D in Fig. 5(a). The 3D fiber pattern, as seen in Fig. 5(b) can be constructed from the 2D convex hull by simply adding the z-dimensions as the mandrel is cylindrical.

4. FEA model

In this study, a global–local submodelling approach is chosen to model the product domain. Here, a course global model is run first to obtain a displacement solution for the entire geometry. These displacements are then applied as boundary conditions on a detailed local 'submodel' in which all relevant effects for the study are modeled to higher fidelity. In such a modeling procedure, it is sufficient to achieve convergence of only the displacement field (as opposed to the full stress field) in the global model as the displacements are the only relevant quantities transferred to the local model. This reduces the computational complexity of the model several-fold due to the relatively few elements needed to obtain an acceptable solution from the global model.

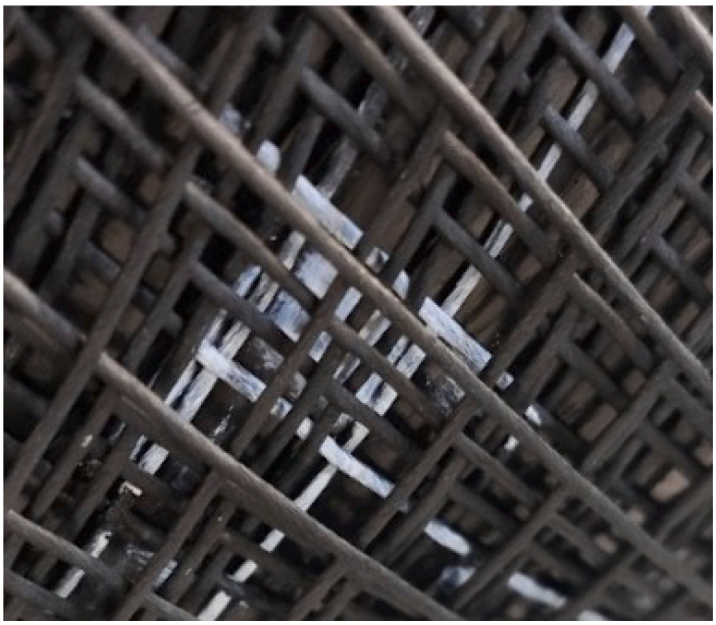

Fig. 4. Fiber build-up during filament winding.

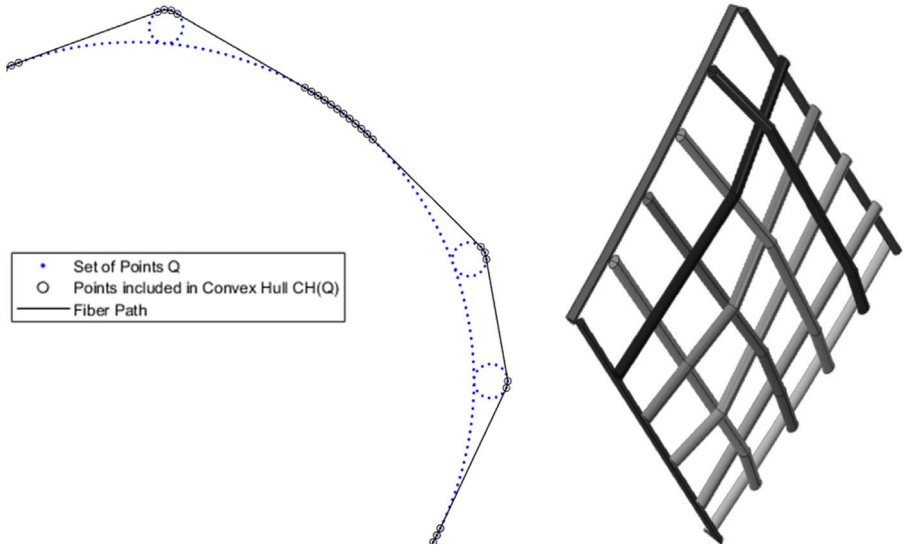

(a) 2D Convex hull algorithm for fiber overlap (fibers not to scale)

(b) Fiber grid with overlapping fibers

Fig. 5. Using the 2D convex hull algorithm to form the 3D fiber RVE.

4.1. Global model

To keep computational costs low in the global model, a homogenization scheme was used to model the fiber layers. Perhaps the most studied homogenization scheme to model the fiber layer in CRC structures is the use of *rebar* layers [33–37]. Here, a fully anisotropic continuum is created for the fiber layer based on material properties, fiber angles, and fiber spacings defined by the user [38]. Using this technique, regions with uniform fiber spacing, fiber angles, and fiber cross-sections can be represented as a singular rebar section.

Choosing the rebar homogenization approach has several advantages:

- It has the capability to represent complex filament winding parameters using only three parameters.
- There is independent modeling of the rubber and fiber allowing each component to be modeled with its own representative material model.
- Rebar allows for hyperelastic material models to be used in its material definitions.
- General non-orthogonal fiber angles can be defined using this method, thus defining a fully anisotropic medium.
- In non-linear analyses under large displacements, rebar accounts for the change in fiber cross-sectional areas, fiber angles, and fiber spacings. This means that the rotation of the fibers represents actual deformation, and hence should be able to capture key phenomena such as fiber scissoring and realignment.

The global model is created as seen in Fig. 6. The product to be modeled is symmetric about its axis and also about its length. This

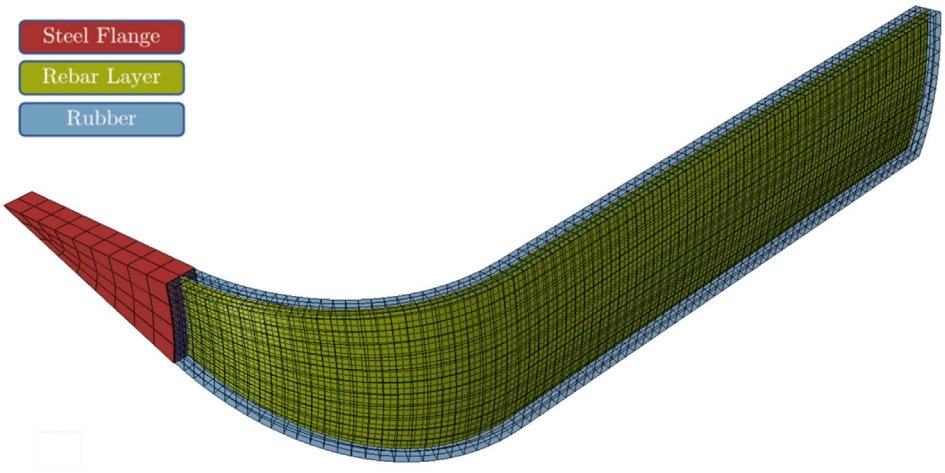

Fig. 6. Global Model.

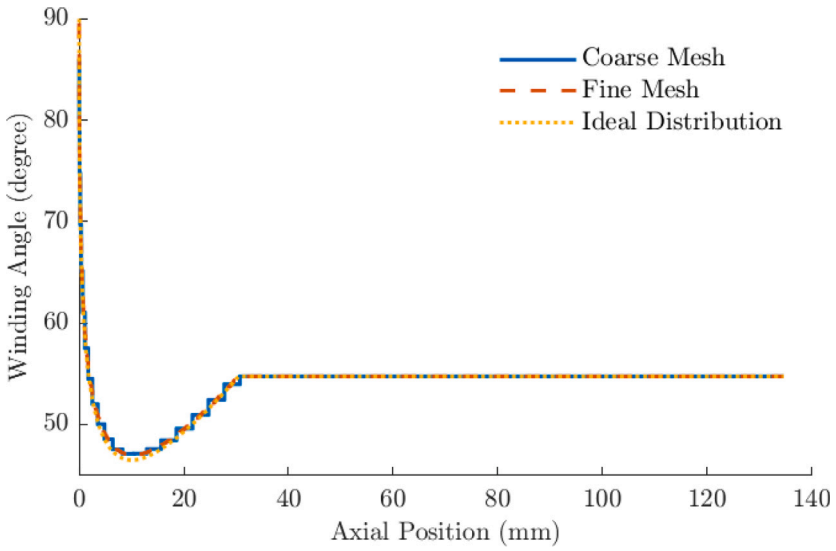

Fig. 7. Discretization of winding angles in the rebar mesh.

allows the creation of a greatly reduced global model with symmetry about both the Z and the θ axes.

The rebar layer is created via a Python script that interpolates the fiber winding angles from the TaniqWind program to create a discrete element-wise angle distribution as seen in Fig. 7. This rebar layer is then constrained within the rubber elements using the ABAQUS embed constraint, which constrains the nodal displacements of the rebar layer based on the displacements of neighboring rubber element nodes. Interfacial effects are not accounted for in the global model since this model's primary aim is to capture the displacement response.

The rubber and flange elements are modeled using linear solid hybrid C3D8H elements, while the rebar is modeled using linear 3D surface elements (SFM3D4).

4.2. Local model

For the local model, a rhomboidal RVE is created using the fiber overlap pattern shown in Fig. 5(b) by adding a rubber layer around it. Linear hybrid tetrahedral elements (C3D4H) were used to mesh the rubber, while quadratic hybrid wedge elements (C3D15H) were used to mesh the fibers. Wedge elements were specially chosen for the fiber as they can mesh circumferentially about the central axis of each fiber — see Fig. 8. This is desirable as material data for transverse deformation of the fiber is not available, and thus capturing fidelity in this direction by increasing mesh density is not beneficial.

4.3. Submodelling implementation

The results of the global model are linked to the local model via a one-way submodelling approach. Feedback from the local to the global model was not deemed necessary due to the near-simultaneous failure of all the fibers in the submodel.

It was noticed that the ABAQUS submodelling implementation was not always consistent in its boundary condition extrapolation from the global model to the local model, leading to spurious displacement at some nodes and causing non-convergence. To combat the above issue, a novel implementation of the submodelling approach was created. Here, the local model boundary mesh is copied via a MATLAB script to form a surface mesh (SFM3D3/SFM3D4 elements) in the global model. This boundary mesh is then placed in the global model at the correct location via the embed constraint — see Fig. 9. The role of this surface mesh is to act as a $1:1$ representation of the local model within the global model and collect the boundary displacements. Having no material assignment, this surface mesh is free to deform without resistance according to the surrounding conditions in the global model. The final displacements of this surface can then

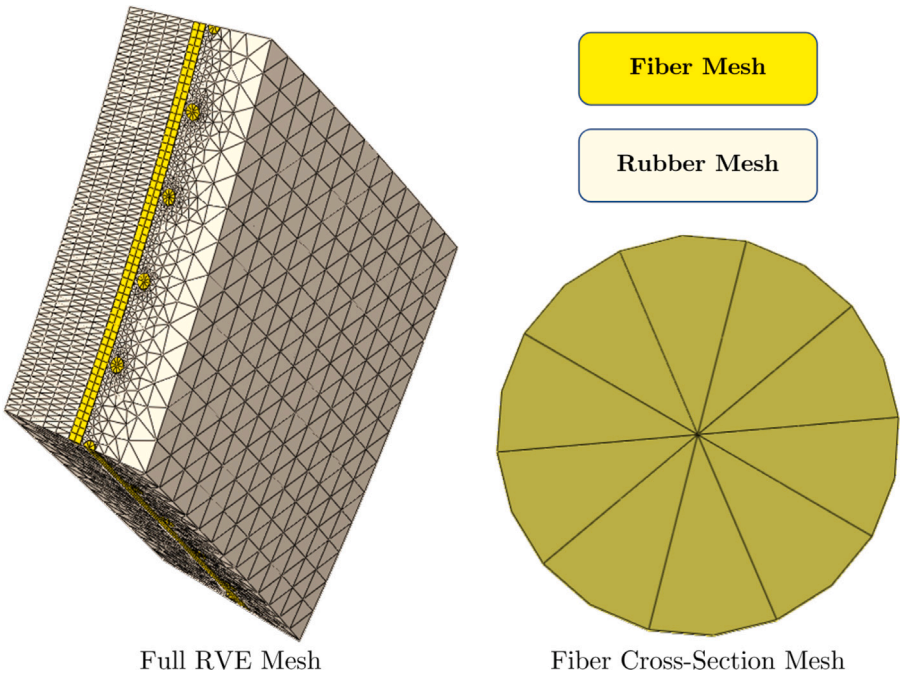

Fig. 8. Rhomboidal submodel mesh.

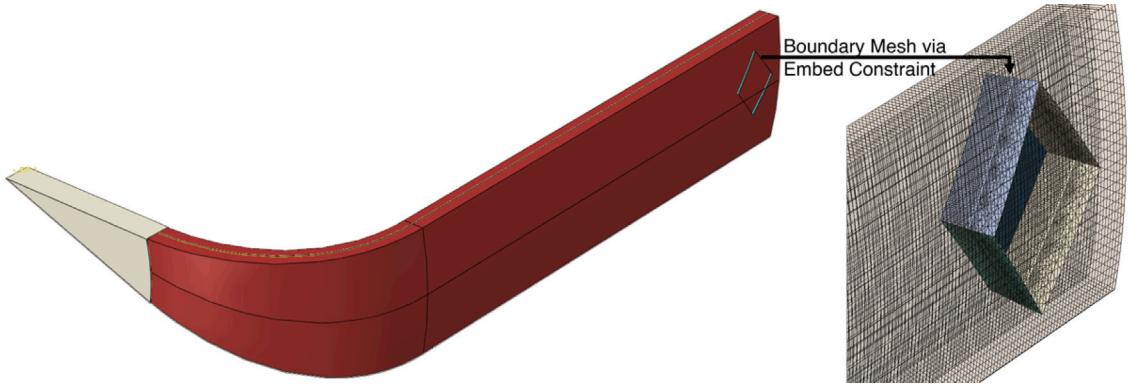

Fig. 9. Positioning of surface mesh within global model using embed constraints.

be applied as boundary conditions to the local model without any transformation or interpolation.

5. Implementing damage

5.1. Damage modes

Fiber damage is the principal source of damage in CRC structures [39–41]. This is especially true in filament wound structures, in which stress concentrations near fiber overlaps are a key cause of fiber failure [14,17].

Natural rubber, with a failure strain usually exceeding 100%, is unlikely to undergo tensile failure in the strain regime expected in this study. Additionally, even rubber shear-banding [42–47], which is an important failure mode in open-ended CRC structures, is irrelevant for this study considering the rubber has no 'free-ends' due to its geometry. Hence, rubber damage is not modeled in this study. Modeling of any low-strain damage effects arising due to cyclic loading, such as Mullins damage[48], is not within the scope of this project.

Fiber-rubber interfacial debonding is another common failure mechanism in cord-rubber composites. The most prevalent type is fiber 'socketing,' where a cylindrical debond grows along the length of the fiber at the cord-rubber interface [20,41,42,46]. This type of interfacial damage is particularly concerning under cyclic or fatigue loads, as initial debonding sources are amplified over repeated cycles, ultimately compromising the load path through the fibers. However, since this project focuses on single-cycle burst testing, the additional computational cost of modeling the interfacial damage, e.g. via cohesive seams, and the additional experimental cost of characterizing the traction-separation law, are not justified within the study's scope.

5.2. Damage criteria

Noting that only the uniaxial tensile behavior of the fibers has been studied via tensile tests, a failure criterion that relies only on field variables in this direction is considered appropriate. Thus, a simple maximum axial strain (ϵ_{11}) failure criteria was used for the fibers. Based on the averaged results (Fig. 2(b)) of the tensile experiments, the uniaxial failure strain of the fibers is 0.21108.

To define the axial direction of the undulating fibers in the local model, unique local material coordinate systems were defined for each fiber element using a Python script. The maximum strain criteria itself was implemented using the user subroutine — USDFLD [49] to numerically delete elements above the prescribed strain limit.

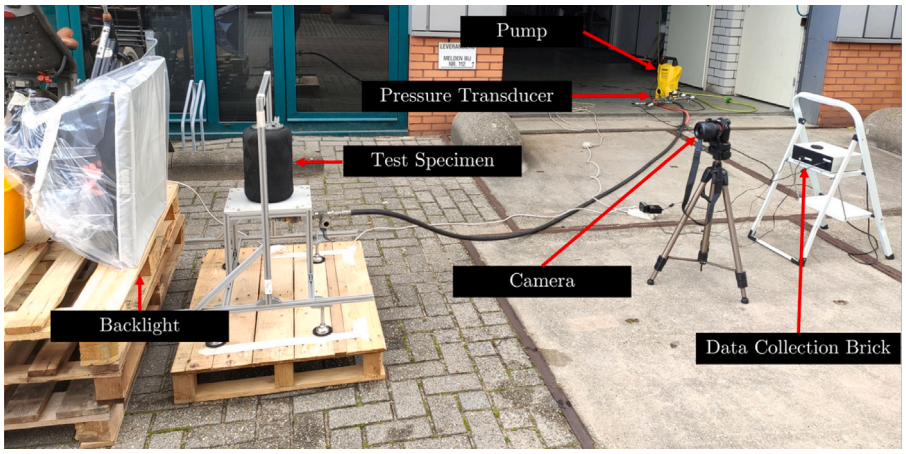

Fig. 10. Burst pressure testing setup at TANIQ BV.

The local model is considered failed at the first occurrence of fiber failure. It must be kept in mind that as the local model is an RVE of a repetitive rhombus, its failure would represent the simultaneous fiber failure in these rhombi around the cylinder. Thus, the failure of the first fiber in the rhombus is not equivalent to the failure of only the first fiber in the product as a whole, but rather as a failure of an equivalent *volume-fraction* of fibers across the product domain.

5.3. Effect of submodelling on damage model

Transfer of boundary conditions using the submodelling approach as described poses a unique deformation state in the local model close to the boundary. In this region, the fibers show especially high transverse deformation. This can be explained by the fact that the global model has only a 2D rebar layer representing the fibers. Thus, all the boundary conditions are transferred to the local model from the deformation of the rubber elements only. Since these rubber elements are orders of magnitude softer than the fiber, the displacements are proportionately large, thus causing this effect.

Fortunately, these boundary effects are extremely local, and die out within only a few elements. To ensure that the damage model is not affected by the deformation of these elements, these boundary elements are excluded from the damage analysis.

6. Experimental setup

The results of the FEA model were compared against burst tests of experimental demonstrators produced at TANIQ BV. Data from 4 demonstrators is used for the comparison.

Experimental burst specimens were secured on a test rig as shown in Fig. 10 and then were pressurized internally with water using a pump. Photographic measurements were used to obtain the axial and diametrical displacements using a Sony Alpha 7S digital camera. To obtain a continuous log of internal pressure within the product, an RS-Pro 0–40 bar analog pressure transducer was used. An Arduino-Uno based digital data collection brick was created to collect the data from the camera and the pressure sensor. The analog inputs from the laser and pressure sensors were converted to digital signals using a 16-bit ADC, while a digital switch controlled the shutter click of the camera automatically. The data streams from the camera and the pressure transducer were synchronized using an onboard real-time clock (RTC) module and then were stored on an SD card in real time as a .csv file. The setup as constructed on site is seen in Fig. 10.

6.1. Measurements via image processing

For the specimen measurements, an image processing script was written in MATLAB that extracted the boundary of the specimen from a high-contrast image taken by the data collection brick — see Fig. 11. To create sufficient contrast, a high-intensity backlight was used as seen in Fig. 10. The image was further binarised in MATLAB to get a crisp boundary definition. Horizontal and vertical rulers present on the test-rig frame helped to calibrate distances from pixels to mm.

Using data from four specimens, the average burst pressure for the design was ascertained to be 14.23 bar (Fig. 14).

7. Results

7.1. Global model performance

The rebar layer strain in the global model at the expected burst pressure of 15.13 bar is shown in Fig. 12(a). One of the main observations here is the equally loaded cylindrical section, which satisfies the criteria for the applicability of the RVE modeling philosophy.

Using the setup described in Section 6, the axial and diametrical displacements of the demonstrators were compared against those of the global model. This was to ensure that the global model was passing on accurate displacements to the local model.

The comparison between the maximum diameters of the demonstrator and the FEA model with varying internal pressure is seen in Fig. 12(c). In terms of diametrical errors, an excellent correlation is seen, with a maximum deviation of 1.13% at lower pressures. A similar plot is seen in Fig. 12(b) for the comparison between experimental and global model flange-to-flange axial elongation. Again, excellent correlation is seen with the maximum deviation being 2.49% at pressures close to bursting.

Thus, it can be shown that the rebar model can capture the global displacements with sufficient fidelity to serve as the boundary conditions for the local model.

An interesting question to address is the performance of the global model alone in predicting the burst pressure of the specimen. It can be theorized that the global model should overpredict the strength of the product since it does not consider the effect of overlaps. This is indeed observed, with the rebar in the global model reaching a maximum principle strain of only $\approx 14\%$ at the expected burst pressure of 14.23 bar, which is a $\approx 33\%$ overprediction in the strength of the vessel. This motivates the need to use the local model along with the global model.

(a) Image from camera (b) Binarised image

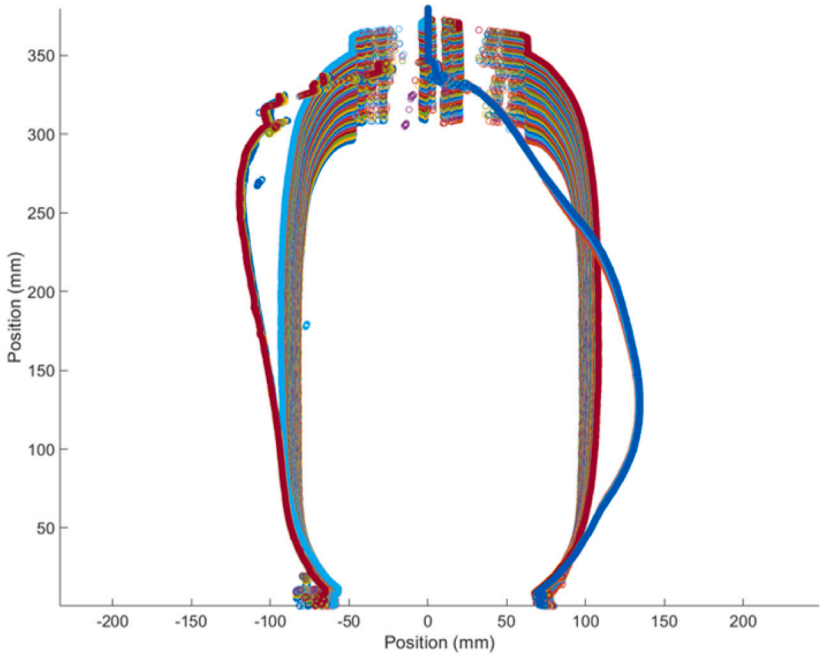

(c) Obtained boundaries from all images

Fig. 11. Specimen deformation measurements via image processing.

7.2. Local model burst pressure prediction

The progression of fiber failure in the local model is now discussed. Initially, stress peaks are formed near the fiber overlap regions due to local restrictions on deformation - see Fig. 13(a). Here, a kinked fiber is unable to straighten out under the applied load due to the presence of a fiber under it, thus causing stress concentrations on both the participating fibers. Once the fiber elements in this overlap region reach the critical axial strain, they fail, causing a local stress drop — see Fig. 13(b). Finally, the failure of some fibers causes accelerated loading of the other fibers, leading to a near-simultaneous failure of multiple fibers in Fig. 13(c).

To check the accuracy of the solution, the burst pressure obtained using the FEA model was compared against failure pressures from experimental burst tests. Fig. 14 shows the experimental burst pressures of four CRC prototypes, having an average burst pressure of 14.23 bar. In comparison, the FEA model predicts the burst pressure to be 15.13 bar.

This error of 6.3% is already an acceptable solution within engineering precision. The over-prediction of the burst pressure may be due to:

- Non-inclusion of structural softening due to interface damage.
- Assumption of an isotropic material model for the twisted cord that is inherently much softer in the transverse direction.

The local model had a significantly longer wall-clock runtime compared to the global model, averaging 8 times longer to complete on the same hardware and CPU count. Therefore, it is recommended to use the global model for preliminary design analysis. The combined global–local approach should be reserved for evaluating final design contenders and products where safe operation is crucial.

7.3. Fiber scissoring

To validate the ability of the model to capture relevant physical phenomena such as fiber scissoring during deformation, an additional winding angle of $\alpha = 45°$ was chosen and recreated in the FEA model. Until now, a neutral angle ($\alpha_n \approx 54.74°$) was used for this project which allowed minimal fiber reorientation. Any fiber winding pattern whose angle deviates from this angle will experience fiber reorientation upon loading such that it tends towards the neutral winding angle. The aim

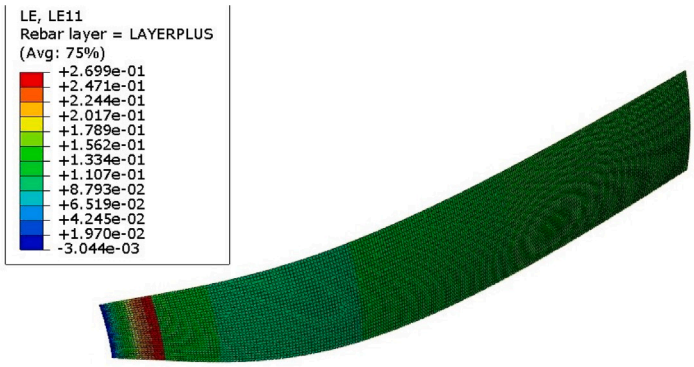

(a) Rebar layer strains at burst pressure (14.23 bar) are constant in the the cylindrical region

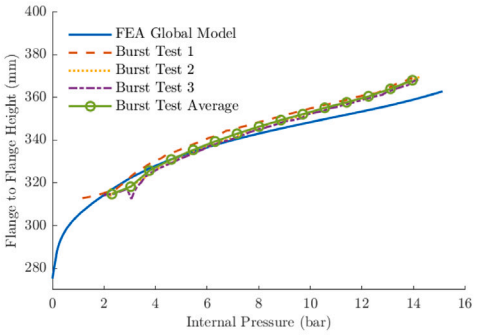

(b) Flange to flange height comparison between global model and experiment

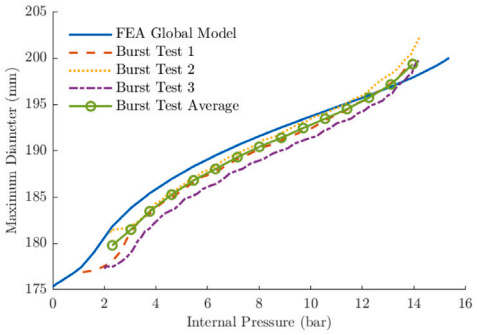

(c) Maximum diameter comparison between global model and experiment

Fig. 12. Global model performance against experimental data.

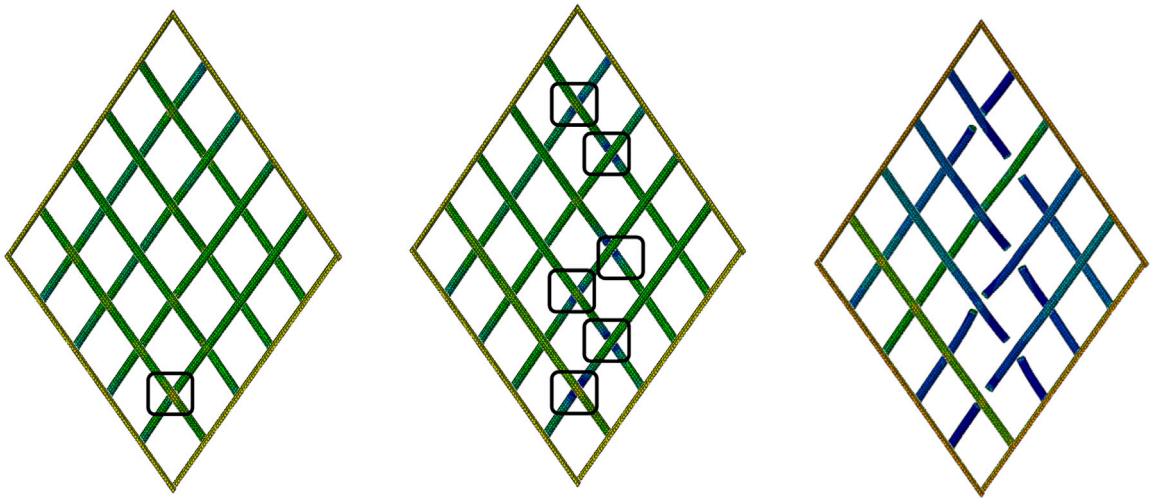

(a) Initial strain concentrations at overlap zones

(b) Near-simultaneous fiber failure initiation

(c) Complete fiber failure

Fig. 13. Local model fiber damage sequence.

is to ascertain that this mechanism is captured by the proposed FEA model.

The fiber scissoring behavior was studied for both the local and the global models. In Fig. 15, it can be seen that on pressurizing the sample, there is a rapid reorientation of the fibers towards $\alpha \approx \alpha_n$. During this period, the fiber strains are comparatively low, with most of the deformation being rigid body rotation. Once the fibers are reoriented, they rapidly take up the load, seen in the sudden change in the slope of the strain curve at around 1.5 bar.

A similar reorientation can also be seen in the local model. Here, the angle is measured using the 2D projected image of the fibers as seen in Fig. 16(b).

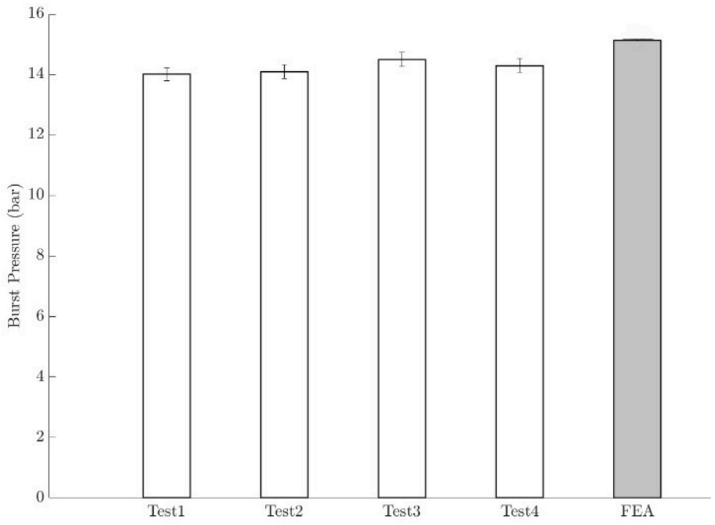

Fig. 14. Comparison of experimental and FEA burst pressures — FEA highlighted in gray.

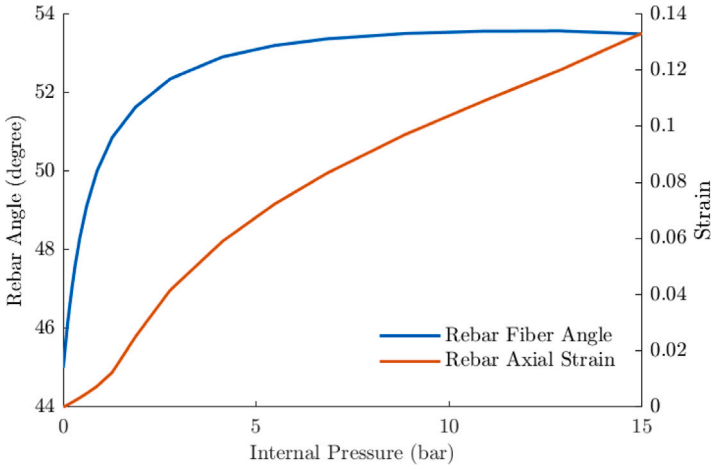

Fig. 15. COLOR PRINT NEEDED: Variation of global model fiber angles and strains with pressure in the cylindrical region.

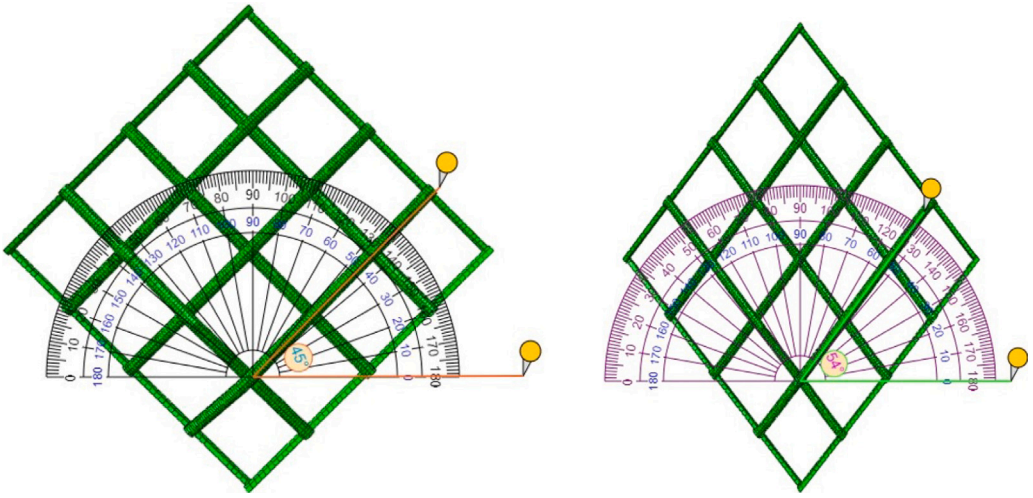

(a) Pre-deformation (b) Post-deformation

Fig. 16. Fiber scissoring in local model.

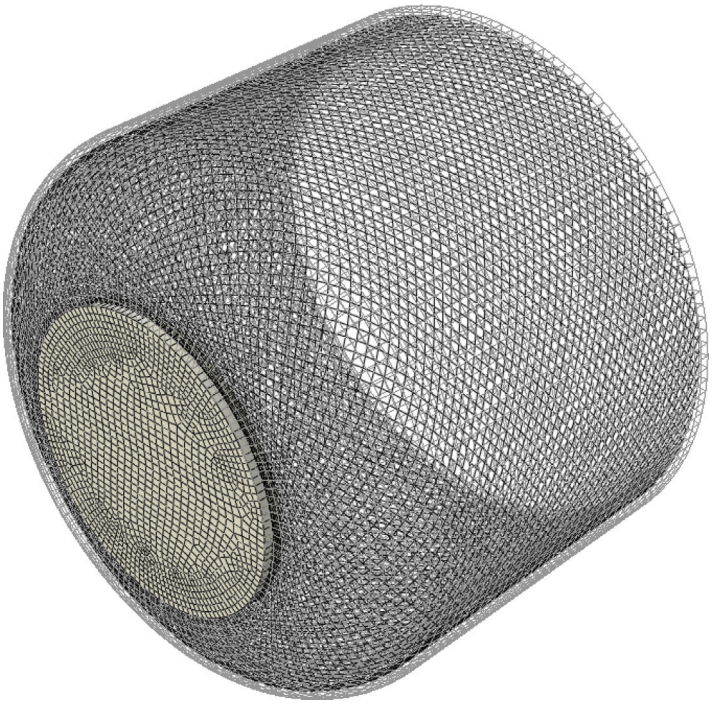

Fig. 17. Half CRC model without fiber overlap using truss elements. Rubber elements are made transparent here to highlight the fiber layer.

8. Effect of fiber overlap

The motivation to model the overlapping fiber geometry in the FEA model has up until now been sourced from literature (see Section 1), and experimental observations. However, with the development of the model, a direct comparison can be made between the burst pressures of a model with and without a fiber overlap pattern.

The most common method of modeling fibers in a matrix has been the use of truss elements [50–52]. Using truss elements, the fiber pattern can pre reproduced perfectly by aligning the truss elements with the fiber directions.

Fig. 17 shows the developed truss model. Here, instead of fiber overlaps, intersecting fibers share a common node at the intersection point.

This truss model, using a similar first-fiber failure criteria, overshoots the experimental average burst pressure by $\approx 26.7\%$, compared to the $\approx$ 6.3% in the developed model. This validates the need to model the fiber overlap geometry to obtain accurate stress states in filament-wound rubber structures.

9. Conclusion

In this paper, the single-cycle burst pressure of cord-reinforced rubber composite pressure vessels was studied using a multiscale submodelling approach using an FEA model. The achieved results improve the burst pressure prediction error from 33% using global-only modeling methods to $\approx 6\%$ using a combined global–local FEA approach.

This paper highlights the need to model the fiber overlap pattern in filament-wound (rubber) composite structures and proposes a global–local submodelling methodology to analyze the burst pressure of these structures using finite element analysis. Experimental burst tests were carried out, which highlighted that the proposed model can capture key phenomena such as fiber reorientation on loading and macroscopic deformations. Additionally, the model can improve the burst pressure prediction several-fold over conventional fiber modeling methods using truss elements. Future improvements may focus on including a two-way submodelling approach to study the progressive failure of fibers, including cohesive seams to study the effect of interfacial degradation on the burst pressure, and using anisotropic hyperelastic models for the twisted cords to better capture their architecture.

Several improvements can be suggested to the proposed model to improve the feasibility of the model to capture additional damage modes, allow propagation of damage post initial-damage, and increase the fidelity of the representative volume region. These are presented in the following paragraphs.

Filament wound fiber-bundles are usually wound under tension. This means that overlapping fibers exert compaction forces on underlying fibers due to their orientation and tension. The simplified convex-hull model presented in this paper discounts this behavior by treating the problem purely geometrically. Instead, bridged sections of the fiber can be treated as beams (see Fig. 18(b)) - on which bending forces resulting from overlapping fibers can be applied. These can be solved analytically for a more accurate representation of the filament wound patterns.

Another limitation of the current model is its inability to predict progressive failure. The current implementation of the submodelling approach is one-way, which implies that there is no feedback from the local model back to the global model. For the specimens studied in this project, there was a sudden failure, thus negating the need to model progressive failure. However, in structures where damage is progressive, the proposed model can be modified as shown in Fig. 19.

To capture the complete stress triaxiality in the cords, a more refined material model for the fibers may also be used. The Marlow hyperelastic material model used to describe the fiber material response in this is an isotropic one, but studies have shown that there are as many as four orders of magnitude differences in the axial and transverse moduli of twisted cord constructions [36]. To overcome this hurdle, simple transversely isotropic hyperelastic material models, as described by Spencer [4,53] may be used to model the fiber bundles. However, experimentally characterizing the transverse properties of the cord can be a challenging affair.

Finally, one of the main components missing in the current study is the effect of initial conditions. These initial conditions are the effect

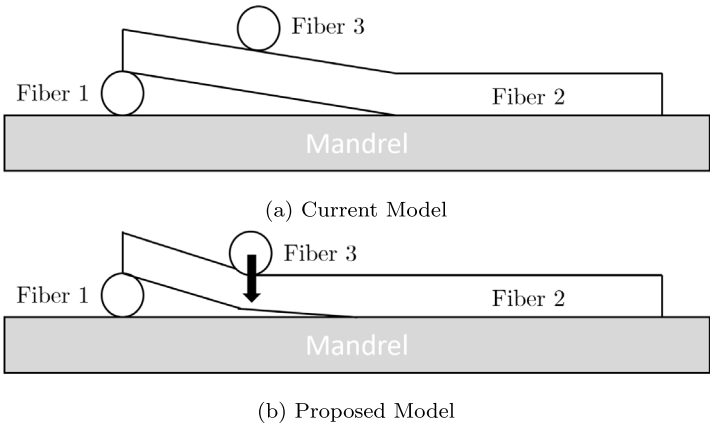

Fig. 18. Comparison of fiber overlap geometry between current and proposed models.

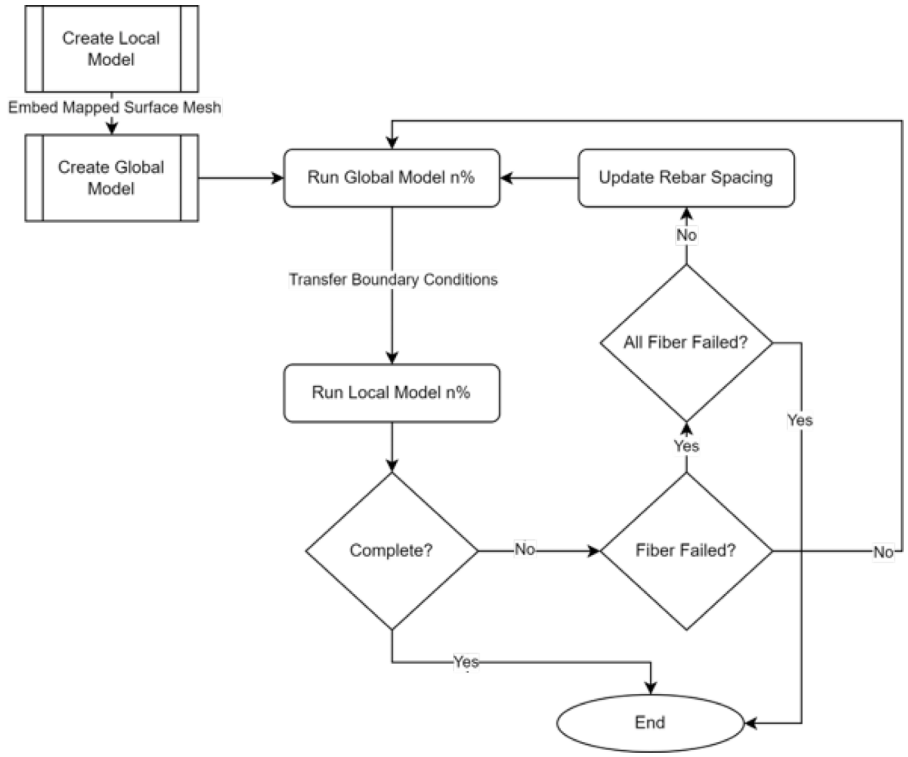

Fig. 19. Possible workflow for implementing a two-way submodel with progressive fiber failure.

of the production parameters, which are influenced by the filament winding process and vulcanization in the oven. Some important effects not considered in this study include:

1. Effect of the initial stress state in the fibers due to winding under tension.
2. Effect of fiber deviation due to fiber slippage and winding with multiple fibers (see Fig. 20).
3. Stochastic analysis of defects, such as voids and regions of under-cured rubber.

Funding

This research did not receive any specific grant from funding agencies in the public, commercial, or not-for-profit sectors.

CRediT authorship contribution statement

Ahaan Bhosale: Writing – original draft, Software, Methodology, Investigation, Conceptualization. **Rob Barendse:** Writing – review & editing, Supervision, Conceptualization. **Boyang Chen:** Writing – review & editing, Supervision, Conceptualization. **J.M.J.F. van Campen:** Writing – review & editing, Supervision, Conceptualization.

Declaration of competing interest

The authors declare that they have no known competing financial interests or personal relationships that could have appeared to influence the work reported in this paper.

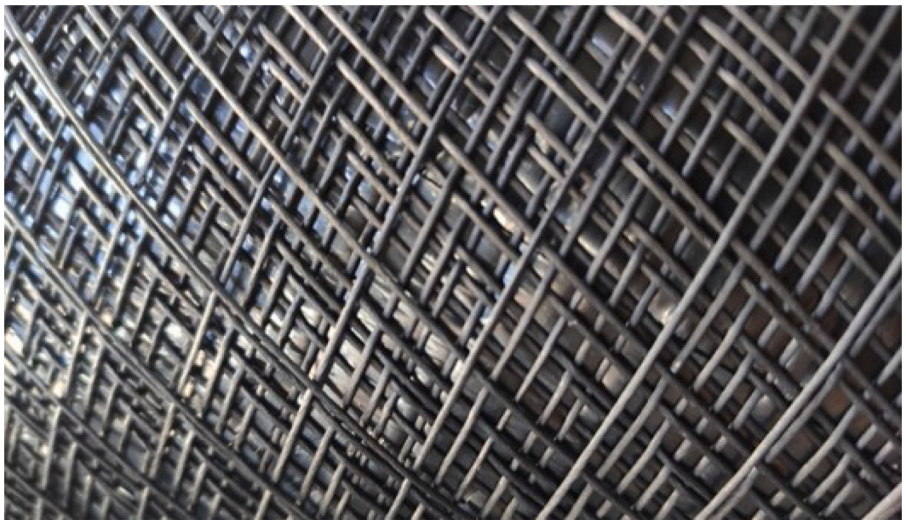

Fig. 20. Uneven spacing between fibers due to slippage. Slippage occurs either due to insufficient friction, or because the winding program does not account for radial buildup during the winding process.

Data availability

The necessary data required to replicate the findings presented in the manuscript may be made available on request.

References

[1] Akasaka T, Hirano M. Approximate elastic constants of fiber reinforced rubber sheet and its composite laminate. Compos Mater Struct 1972;1:70–6.

[2] Clark S. The plane elastic characteristics of cord-rubber composites. Tech. rep., Ann Arbor: The University of Michigan Research Insitute; 1960.

[3] Ford J, Patel H, Turner J. Interlaminar shear effects in cord-rubber composites. Fibre Sci Technol 1982;17(4):255–71. http://dx.doi.org/10.1016/0015-0568(82)90021-5.

[4] Spencer AJM. Constitutive theory for strongly anisotropic solids. Courses and lectures - International centre for mechanical sciences, (282):1984, p. 1–32. http://dx.doi.org/10.1007/978-3-7091-4336-0_1.

[5] Holzapfel GA, Gasser TC, Ogden RW. A new constitutive framework for arterial wall mechanics and a comparative study of material models. J Elasticity 2000;61(1–3):1–48. http://dx.doi.org/10.1023/A:1010835316564.

[6] Nguyen NH, Raatschen H-j, Staat M. A hyperelastic model of biological tissue materials in tubular organs. In: IV European conference on computational mechanics, no. May. Paris: Center for Research and Technology Hellas; 2010.

[7] Peng XQ, Guo ZY, Moran B. An anisotropic hyperelastic constitutive model with fiber-matrix shear interaction for the human annulus fibrosus. J Appl Mech Trans ASME 2006;73(5):815–24. http://dx.doi.org/10.1115/1.2069987.

[8] Peng X, Guo G, Zhao N. An anisotropic hyperelastic constitutive model with shear interaction for cord-rubber composites. Compos Sci Technol 2013;78:69–74. http://dx.doi.org/10.1016/j.compscitech.2013.02.005.

[9] Peng X, Guo Z, Du T, Yu WR. A simple anisotropic hyperelastic constitutive model for textile fabrics with application to forming simulation. Composites B 2013;52:275–81. http://dx.doi.org/10.1016/j.compositesb.2013.04.014.

[10] Aboshio A, Green S, Ye JQ. New constitutive model for anisotropic hyperelastic biased woven fibre reinforced composite. Plast Rubber Compos 2014;43(7):225–34. http://dx.doi.org/10.1179/1743289814Y.0000000097.

[11] Xu X, Yao X, Dong Y, Yang H, Yan H. Mechanical behaviors of non-orthogonal fabric rubber seal. Compos Struct 2021;259(November 2020):113453. http://dx.doi.org/10.1016/j.compstruct.2020.113453.

[12] Yang H, Yao XF, Ke YC, Ma Yj, Liu YH. Constitutive behaviors and mechanical characterizations of fabric reinforced rubber composites. Compos Struct 2016;152:117–23. http://dx.doi.org/10.1016/j.compstruct.2016.05.021.

[13] Morozov EV. The effect of filament-winding mosaic patterns on the strength of thin-walled composite shells. Compos Struct 2006;76(1–2):123–9. http://dx.doi.org/10.1016/j.compstruct.2006.06.018.

[14] Rousseau J, Perreux D, Verdière N. The influence of winding patterns on the damage behaviour of filament-wound pipes. Compos Sci Technol 1999;59(9):1439–49. http://dx.doi.org/10.1016/S0266-3538(98)00184-5, URL https://linkinghub.elsevier.com/retrieve/pii/S0266353898001845.

[15] Shen C, Han X, Guo Z. A new method for calculating the stiffness of filament wound composites considering the fibre undulation and crossover. Adv Compos Lett 2014;23(4):096369351402300. http://dx.doi.org/10.1177/096369351402300402, URL http://journals.sagepub.com/doi/10.1177/096369351402300402.

[16] Yin DM, Li BM, Ch Xiao H. Prediction of three-dimensional elastic behavior of filament-wound composites based on the bridging model. J Phys Conf Ser 2020;1507(6):62008. http://dx.doi.org/10.1088/1742-6596/1507/6/062008, URL https://iopscience.iop.org/article/10.1088/1742-6596/1507/6/062008.

[17] Zhang Y, Xia Z, Ellyin F. Two-scale analysis of a filament-wound cylindrical structure and application of periodic boundary conditions. Int J Solids Struct 2008;45(20):5322–36. http://dx.doi.org/10.1016/j.ijsolstr.2008.05.026.

[18] Pidaparti RMV. modelling and fracture prediction in rubber composites [Ph.D. thesis], West Lafayette: Purdue University; 1989.

[19] Pidaparti RMV, Yang HTY, Soedel W. Modeling and fracture prediction of single ply cord-rubber composites. J Compos Mater 1992;26(2):152–70. http://dx.doi.org/10.1177/002199839202600201.

[20] Jha NK, Nackenhorst U. Fatigue mechanisms of cord-rubber composites. Pamm 2015;15(1):133–4. http://dx.doi.org/10.1002/pamm.201510057.

[21] Jha NK, Nackenhorst U. Fatigue life prediction of cord–rubber composite structures based on progressive damage analysis. Eng Comput (Swansea, Wales) 2018;35(6):2215–33. http://dx.doi.org/10.1108/EC-12-2016-0450.

[22] Jha NK. modelling and numerical simulation for the prediction of the fatigue strength of airsprings [Ph.D. thesis], Universität Hannover; 2018.

[23] Walter JD. Cord—Rubber tire composites: Theory and applications. Rubber Chem Technol 1978;51(3):524–76. http://dx.doi.org/10.5254/1.3535749.

[24] Koussios S. filament winding: a unified approach [Ph.D. thesis], Delft: TU Delft; 2004.

[25] Peters ST. Composite filament winding. ASM International; 2011.

[26] ASTM International. ASTM D885-10a: Standard Test Methods for Testing Tire Cords , Tire Cord Fabrics , and Industrial Yarns. 2010, p. 1–10.

[27] Bergström J. Elasticity/Hyperelasticity. In: Mechanics of solid polymers. Elsevier; 2015, p. 209–307. http://dx.doi.org/10.1016/B978-0-323-31150-2.00005-4.

[28] Li X, Wei Y, Feng Q, Luo RK. Mechanical behavior of nylon 66 tyre cord under monotonic and cyclic extension: Experiments and constitutive modeling. Fibers Polym 2017;18(3):542–8. http://dx.doi.org/10.1007/s12221-017-6961-x.

[29] Marlow RS. A general first-invariant hyperelastic constitutive model. In: Busfield J, Muhr A, editors. Constitutive models for rubber. London: CRC Press; 2003, p. 157–60.

[30] Okereke M, Keates S. Finite Element Applications. In: Springer tracts in mechanical engineering, Cham: Springer International Publishing; 2018, http://dx.doi.org/10.1007/978-3-319-67125-3, URL http://link.springer.com/10.1007/978-3-319-67125-3.

[31] Lemaitre J. A Course on Damage Mechanics. Nuevos sistemas de comunicación e información. Berlin, Heidelberg: Springer Berlin Heidelberg; 1996, http://dx.doi.org/10.1007/978-3-642-18255-6, URL http://link.springer.com/10.1007/978-3-642-18255-6.

[32] Cormen T, Leiserson C, Rivest R, Stein C. Finding the convex hull. In: Introduction to algorithms. 3rd ed. Cambridge, Massachusetts: MIT Press; 2009, p. 1029–39.

[33] Oman S, Nagode M. On the influence of the cord angle on air-spring fatigue life. Eng Fail Anal 2013;27:61–73. http://dx.doi.org/10.1016/j.engfailanal.2012.09.002, URL https://linkinghub.elsevier.com/retrieve/pii/S1350630712001872.

[34] Wang W, Yan S, Zhao S. Experimental verification and finite element modeling of radial truck tire under static loading. J Reinf Plast Compos 2013;32(7):490–8. http://dx.doi.org/10.1177/0731684412474998, URL http://journals.sagepub.com/doi/10.1177/0731684412474998.

[35] Helnwein P, Liu CH, Meschke G, Mang HA. A new 3-D finite element model for cord-reinforced rubber composites—Application to analysis of automobile tires. Finite Elem Anal Des 1993;14(1):1–16. http://dx.doi.org/10.1016/0168-874X(93)90075-2, URL https://linkinghub.elsevier.com/retrieve/pii/0168874X93900752.

[36] Barry C, Panerai F, Bergeron K, Stapleton S, Sherwood J. Mesomechanical modeling of braided cords. Procedia Manuf 2020;47(2019):162–8. http://dx.doi.org/10.1016/j.promfg.2020.04.163.

[37] Sprenger W, Wagner W. On the formulation of geometrically nonlinear 3D-Rebar-elements using the enhanced assumed strain method. Eng Struct 1999;21(3):209–18. http://dx.doi.org/10.1016/S0141-0296(97)00182-X.

[38] Systèmes D. Rebar modeling in shell, membrane, and surface elements. In: ABAQUS theory manual. 2021.

[39] Rao S, Daniel IM, Gdoutos EE. Mechanical properties and failure behavior of cord/rubber composites. Appl Compos Mater 2004;11(6):353–75. http://dx.doi.org/10.1023/B:ACMA.0000045312.61921.1f.

[40] Michel L, Vadean A, Benoit R. Tire burst phenomenon and rupture of a typical truck tire bead design. Tire Sci Technol 2011;39(4):270–83. http://dx.doi.org/10.2346/1.3672044.

[41] Davids B. Structural analysis of multi-layered filament wound cord-reinforced rubber products [Ph.D. thesis], TU Delft; 2014.

[42] Breidenbach RF, Lake GJ. Application of Fracture Mechanics to Rubber Articles , Including Tyres. Philos Trans R Soc Lond Ser A Math Phys Eng Sci 1981;299(1446):189–202. http://dx.doi.org/10.1098/rsta.1981.0018, URL https://www.jstor.org/stable/36741.

[43] Huang YS, Yeoh OH. Crack initiation and propagation in model cord-rubber composites. Rubber Chem Technol 1989;62(4):709–31. http://dx.doi.org/10.5254/1.3536270, URL https://meridian.allenpress.com/rct/article-abstract/62/4/709/92053/Crack-Initiation-and-Propagation-in-Model-Cord.

[44] Tian Z, Song H, Wan Z, Du X. Fatigue properties of steel cord-rubber composite. J Elastomers Plast 2001;33(4):283–96. http://dx.doi.org/10.1106/17HE-05X2-8WAU-HV92.

[45] Lee BL, Ku BH, Liu DS, Hippo PK. Fatigue of cord-rubber composites: II. Strain-based failure criteria. Rubber Chem Technol 1998;71(5):866–88. http://dx.doi.org/10.5254/1.3538515.

[46] Song J. fatigue of cord-rubber composites for tires [Ph.D. thesis], The Pennsylvania State University; 2004, URL http://cat.inist.fr/?aModele=afficheN&cpsidt=3461717.

[47] Gao J, Yang X, Huang LH, Suo Y. Experimental study on mechanical properties of aramid fibres reinforced natural rubber/SBR composite for large deformation–quasi-static mechanical properties. Plast Rubber Compos 2018;47(9):381–90. http://dx.doi.org/10.1080/14658011.2018.1514480.

[48] Holzapfel G. Nonlinear Solid Mechanics: A Continuum Approach for Engineering Science. 1st ed. John Wiley and Sons; 2000.

[49] Dassault Systèmes. USDFLD. In: ABAQUS user subroutine reference manual. 2021.

[50] Oman S, Nagode M, Klemenc J. Rubber–fibre composite modelling and its influence on fatigue damage assessment. Fatigue Fract Eng Mater Struct 2021;44(2):521–32. http://dx.doi.org/10.1111/ffe.13377.

[51] Reese S. Meso-macro modelling of fibre-reinforced rubber-like composites exhibiting large elastoplastic deformation, vol. 40, 2003, p. 951–80.

[52] Sharma SB, Sutcliffe MPF. A simplified finite element model for draping of woven material. Composites A 2004;35(6):637–43. http://dx.doi.org/10.1016/j.compositesa.2004.02.013.

[53] Spencer AJM. Theory of Invariants. In: Eringen AC, editor. Mathematics. Academic Press; 1971, p. 239–353. http://dx.doi.org/10.1016/B978-0-12-240801-4.50008-X.